RSC Advances

PAPER

View Article Online
View Journal | View Issue

Cite this: *RSC Adv.*, 2017, **7**, 45010

Radiation enhanced uptake of $Hg^0_{(g)}$ on iron (oxyhydr)oxide nanoparticles†

Uday Kurien,[a] Zhenzhong Hu,[b] Heonho Lee,[b] Ashu P. Dastoor[c] and Parisa A. Ariya*[ab]

Received 4th July 2017
Accepted 11th September 2017

DOI: 10.1039/c7ra07401h

rsc.li/rsc-advances

Despite the proposed importance of atmospheric mercury (Hg) cycling, little is known about its heterogeneous chemistry, specifically on ubiquitous dust particle surfaces in the environment. To address this gap in knowledge, we herein report the uptake coefficients for the uptake of $Hg^0_{(g)}$ on iron (oxyhydr)oxides (γ-Fe_2O_3, α-FeOOH, α-Fe_2O_3 and Fe_3O_4) nanoparticles, employed as proxies for reactive components of mineral dust. $Hg^0_{(g)}$-particle interactions were studied in a batch set-up, at ambient pressure (760 ± 5 Torr) and temperatures (295 ± 2 K) with UV and visible irradiation (290 nm ≤ λ ≤ 700 nm). γ-Fe_2O_3, α-FeOOH and α-Fe_2O_3 demonstrated a *ca.* 40–900-fold increase in uptake kinetics upon irradiation, under our experimental conditions. In contrast, uptake kinetics on Fe_3O_4's surface displayed little dependence on irradiation. Relative humidity was shown to inhibit the effect of radiation on the uptake of $Hg^0_{(g)}$ by α-Fe_2O_3. Size distributions, electronic properties, surface area and phase characterization of the iron(oxyhydr)oxide particles were studied to explain the uptake kinetics, and to provide insights into the mechanism of $Hg^0_{(g)}$ loss. The adsorption capacity of $Hg^0_{(g)}$ on α-Fe_2O_3 was determined from the adsorption isotherm fitted with Langmuir, Freundlich and Elovich adsorption models. The implications of the results to atmospheric chemical processes are herein discussed.

1. Introduction

Mercury (Hg) is a top priority contaminant of global interest. Gaseous elemental mercury (GEM, $Hg^0_{(g)}$), the predominant form of atmospheric Hg, has a lifetime of several months to years,[1,2] and can have local, regional and global impacts. It is removed from the atmosphere *via* oxidation and deposition.[3] Following deposition, Hg can be either re-emitted into the atmosphere, or methylated and subsequently bio-magnified, adversely impacting human health.[4] As such, the international Minamata treaty was agreed upon by 128 countries to limit anthropogenic Hg emissions into the environment.[5] The recent withdrawal of the US from the 2015 Paris Agreement, and the consequent reversal of its decision to reduce coal fired plants (the largest point source of anthropogenic Hg emissions) is expected to be potentially detrimental to global Hg mitigation efforts.

Deposition of Hg can occur through wet and dry processes, such as the deposition of particulate bound mercury (PBM).[6] Evidence from atmospheric and global modeling studies suggest that both dry and wet deposition pathways are important to the total deposition of Hg; however, owing to large uncertainties in dry deposition processes, estimates among models differ from each other by as much as a factor of 2 in North America and by an order of magnitude on the global scale.[7] The inability to accurately quantify Hg dry deposition has, in part, been attributed to an incomplete understanding of the underlying physico-chemical processes driving Hg transformations.[6]

Of importance to these transformations, specifically the formation of PBM, are ubiquitous atmospheric aerosols. Despite substantial progress having been made in understanding atmospheric gas phase oxidation reactions of Hg^0,[8,9] and reduction reactions of Hg^{2+} on terrestrial surfaces,[10] little is known about the impact of atmospheric aerosol surfaces on GEM. Published literature has speculated on the uptake of $Hg^0_{(g)}$ by particulate matter in the atmosphere based on observations and theoretical analysis.[11,12] However, to the best of our knowledge, experimental studies on the uptake of $Hg^0_{(g)}$ with such surfaces are scarce.

Mineral dusts are common atmospheric aerosols, capable of acting as condensation nuclei influencing cloud formation, Earth's radiation budget and ultimately climate.[13] Dust particles also provide surfaces for the reaction and uptake of trace atmospheric gases such as organic compounds.[14] Metals and metal oxides are important reactive components of dust

[a]*Department of Atmospheric and Oceanic Sciences, McGill University, 801 Sherbrooke West, Montreal, QC H3A 2K6, Canada. E-mail: parisa.ariya@mcgill.ca; Fax: +1-514-398-3797; Tel: +1-514-398-6931; +1-514-398-3615*

[b]*Department of Chemistry, McGill University, 801 Sherbrooke West, Montreal, QC H3A 2K6, Canada*

[c]*Air Quality Research Division, Environment and Climate Change Canada, 2121, Route Transcanadienne, Dorval, QC H9P 1J3, Canada*

† Electronic supplementary information (ESI) available. See DOI: 10.1039/c7ra07401h

particles. Common metal oxides include those of iron and titanium such as Fe_2O_3, Fe_3O_4 ($Fe_2O_3 \cdot FeO$), FeOOH and TiO_2.[15] These oxides lend mineral dusts photo enhanced reactivity towards gases, such as the catalytic decomposition of O_3 [16] and uptake and nucleation of SO_2 [17] and NO_2.[18] While the uptake of $Hg^0_{(g)}$ on TiO_2 is well documented[19] a similar understanding of the photochemical aging processes on iron oxide surfaces is scarce.

It has been suggested that iron oxide fractions in fly-ash promote adsorption of $Hg^0_{(g)}$ in simulated stack conditions.[20] However, due to high temperatures and the complexity of the feed gas and particulate phase composition, little is known about the nature of $Hg^0_{(g)}$–iron oxide interactions at environmentally relevant conditions, after its emission. There are also recent theoretical investigations into mechanisms of Hg^0–Fe_2O_3 interactions.[21,22] These studies, however, do not address the impact of atmospheric relevant radiation on the reactions, particularly in the lower troposphere which is abundant in dust particles.

The objective of this work was, hence, to study the heterogeneous chemistry, influenced by photochemistry and humidity, of $Hg^0_{(g)}$ on the reactive components of mineral dust and to provide insights on the photochemical aging processes in the troposphere. We performed uptake reactions of $Hg^0_{(g)}$ on the surfaces of α-Fe_2O_3 (hematite), γ-Fe_2O_3 (maghemite), Fe_3O_4 (magnetite) and α-FeOOH (goethite) nanoparticles, used as proxies for the reactive components of mineral dust aerosols.[23] The effects of common atmospheric parameters, such as irradiation and humidity, on the promotion or inhibition of these reactions were examined. Reaction kinetics were evaluated and reported as pseudo first order rate constants (k) and uptake coefficients (γ). We discuss our observations in relation to the particle properties obtained through multiple characterization techniques: Nanoparticle Tracking Analysis (NTA), Transmission Electron Microscopy (TEM), BET surface area, X-Ray Diffraction (XRD), X-ray Photoelectron Spectroscopy (XPS) and UV-Visible Diffuse Reflectance Spectroscopy (UV-Vis DRS). We also examine how our laboratory results may help improve global atmospheric Hg models.

2. Experimental section

The following sections detail the experimental procedures employed for the synthesis and characterization of the nanoparticles, the measurement of adsorption kinetics and adsorption isotherms. We provide detailed descriptions of the reaction chambers, $Hg^0_{(g)}$ measurement techniques, methodology and kinetic models employed to evaluate the impact of radiation and relative humidity on the uptake reactions.

2.1 Characterization of the iron (oxyhydr)oxide particles

2.1.1 Phase characterization of iron (oxyhydr)oxide particles. Complementary analytical techniques were used to characterize the iron (oxyhydr)oxide particles. Iron (oxyhydr)oxide phases were determined with a Siemens D500 X-ray diffractometer equipped with Cu Kα radiation source ($\lambda = 1.5418$ Å). XRD patterns were recorded for $20^\circ \leq 2\theta \leq 70^\circ$ with increments of 0.1–0.5°.

2.1.2 Size distribution of iron (oxyhydr)oxide particles. The sizes and geometries of the individual nanoparticles were characterized with a Philips CM200 TEM operating at 200 kV. Size distributions of aqueous suspensions of the iron (oxyhydr) oxide nanoparticles were obtained with NTA (Malvern NanoSight NS500), equipped with a 532 nm laser and Electron Multiplying Charge Couple Device (EMCCD) camera.

2.1.3 Iron (oxyhydr)oxide bang gap determination. The UV-Vis diffuse reflectance spectra ($\lambda = 250$–800 nm) of the iron (oxyhydr)oxide nanoparticle powders were determined using a Cary 5000 UV-Vis-NIR spectrophotometer equipped with the Praying Mantis accessory for solid powders. Baseline corrections were performed with KBr powder and band gaps were identified from the first derivative ($dF/d\lambda$) of the Kubelka–Munk ($F(R)$) function of reflectance (R).[24] The Kubelka–Munk function is defined as:

$$F(R) = \frac{(1-R)^2}{2 \times R} \quad \text{(E1)}$$

2.1.4 Surface area analysis of iron (oxyhydr)oxide particles. BET surface areas of all heterogeneous phases were obtained by nitrogen adsorption on a TriStar 3000 V6.07 surface area analyzer at 77 K. Duplicate measurements were recorded for each sample.

2.1.5 XPS analysis of iron (oxyhydr)oxide particles. Post reaction iron (oxyhydr)oxide particles were analyzed for Hg using a ThermoScientific K-α XPS. The samples were loaded on carbon tape and placed on a grid for the analysis.

2.2 Uptake and adsorption studies: impact of radiation and relative humidity

2.2.1 Reaction preparation. Experiments were carried out in gas tight 2.0 L and 5.5 L round bottom borosilicate glass reaction chambers. The reaction chambers' inner walls were deactivated with a 5% solution of dimethyldichloro silane (DMDCS) in toluene, to minimize secondary reactions and adsorption of $Hg^0_{(g)}$ onto the glass surfaces, which has been reported in previous studies from this group.[25]

The uptake reactions were monitored by measuring the loss of $Hg^0_{(g)}$ using Electron Ionization (EI) Mass Spectrometry (MS) performed with an Agilent G1540A Gas Chromatograph (GC) in tandem with a Hewlett Packard 5973 mass selective detector. Details of the method are presented in Section S1 of the ESI.† Prior to use, the particles were placed in the chamber and swirled to coat the inner walls of the chamber. The reaction chamber, containing the particles, was evacuated to $\sim 5 \times 10^{-2}$ Torr, for 30 minutes, filled with extra dry air and then evacuated again. The process was repeated thrice, using a ChemGlass vacuum line fitted with an Edwards high vacuum pump and Edwards 2 stage pressure gauge, to maximize removal of surface adsorbed species prior to $Hg^0_{(g)}$ uptake experiments.

Quantitative transfer of $Hg^0_{(g)}$ into the reaction chamber was achieved by connecting stock flask (containing $Hg^0_{(l)}$ in

equilibrium with $Hg^0_{(g)}$ in extra dry air) to the vacuum line and allowing $Hg^0_{(g)}$ to diffuse to the evacuated reaction chamber. The amount of $Hg^0_{(g)}$ transferred to the reaction chamber was controlled by tuning the pressure of the reaction chamber relative to that of the stock flask, maintained at ~760 Torr. The final pressure of the reaction chamber was brought upto 760 ± 3 Torr with extra dry. The experiments were performed with an initial $Hg^0_{(g)}$ concentration of 3 μg L^{-1} (±10%).

2.2.2 Humidity and radiation studies. Water vapor was quantitatively transferred into the reaction chamber, from a stock flask containing liquid water. The humidity within the reaction chamber was determined from the vapor pressure of water measured by the Edwards 2 stage pressure gauge.

The order in which the reactants were introduced into the chamber was: (1) the particles, (2) water vapor, (3) $Hg^0_{(g)}$ in air and finally (4) air as the make-up gas to raise the final pressure up to 760 Torr. The start time of the experiment ($t = 0$ minutes) is defined as the time when iron (oxyhydr)oxide particles, $Hg^0_{(g)}$, water vapor and the make-up gas were present in the chamber at 760 Torr.

The reaction chamber was housed in an irradiation chamber equipped with appropriate broadband illumination sources for UV-A ($315 \leq \lambda \leq 400$ nm), UV-B ($280 \leq \lambda \leq 315$ nm) and visible ($400 \leq \lambda \leq 700$ nm) radiation. Details of the light sources and characterization of their radiation intensity and emission spectra are presented in Section S2 of the ESI.† The temperature of the irradiation chamber was monitored using a Fischer Scientific temperature probe.

2.2.3 Calculation of uptake coefficient. In accordance with other batch studies on heterogeneous and uptake reactions,[26,27] the apparent rate constants (k) for the loss of $Hg^0_{(g)}$ on fixed mass loadings of the particles were calculated assuming pseudo first order kinetics,[28,29] by monitoring the change of concentration of $Hg^0_{(g)}$ ($[Hg]_t$) with time (t) according to the equation:

$$\ln[Hg]_t = k \times t + \ln[Hg]_o \quad \text{(E2)}$$

where, $[Hg]_o$ is the concentration of $Hg^0_{(g)}$ at $t = 0$. Kinetic experiments were repeated at least thrice with the error bars representing the standard deviation of the trials.

The pseudo first order rate constant (k) was expressed as the uptake coefficient (γ) defined as:[30]

$$\gamma = \frac{4k}{\nu_{Hg} S_{BET} C_{mass}} \quad \text{(E3)}$$

where, S_{BET} and C_{mass} are the BET surface area and mass loading of the sorbent, respectively and ν_{Hg} is the mean velocity of $Hg^0_{(g)}$ atoms.

Additionally, the statistical significance of the effect of radiation on $Hg^0_{(g)}$ loss was calculated by comparing sample means of $Hg^0_{(g)}$ concentrations post irradiation to $Hg^0_{(g)}$ concentrations in control (dark) experiments using the 2 sample Student t-test with the Welch correction, to account for different sample sizes and variances. The t-tests were executed using the default algorithms in R programming language. A p value of less than 0.05 was used to identify statistically distinct samples in a 95% confidence interval.

2.2.4 Adsorption isotherm. The isotherm for the adsorption of $Hg^0_{(g)}$ on the surfaces of α-Fe_2O_3 was determined in 5.5 L flasks with dry air and visible light at 22.3 ± 2 °C. Initial $Hg^0_{(g)}$ concentrations were kept constant (3 μg L^{-1} ± 10%) while α-Fe_2O_3 dosage was varied (0.0034–0.5000 g L^{-1}). From the adsorption curves, the time taken to attain equilibrium was found to be approximately 30–36 hours. The system was allowed to equilibrate for an additional 12 hours to maximize surface coverage of α-Fe_2O_3. Langmuir, Freundlich and Elovich adsorption models were fit to the experimental data. The goodness of fits for each model was evaluated per their coefficient of determination (R^2) in their linearized forms. Sources of experimental uncertainties are discussed in Section S3 of the ESI.†

2.3 Materials and supplies

2.3.1 Synthesis of Fe_3O_4 and α-FeOOH. Fe_3O_4 was synthesized using the method described by Massart.[31] Briefly, ammonium hydroxide (NH_4OH) was added dropwise to a 2 : 1 solution of ferric chloride hexahydrate ($FeCl_3 \cdot 6H_2O$) and ferrous chloride tetrahydrate ($FeCl_2 \cdot 4H_2O$) in deoxygenated water maintained at 85 °C. The nanoparticles were recovered magnetically and rinsed thrice with warm deoxygenated water and allowed to dry in a vacuum oven maintained at 60 °C. The synthesized nanoparticles were stored in a vacuum desiccator for the duration of the experiments to minimize oxidation by atmospheric O_2.

α-FeOOH nanoparticles were prepared by adding sodium hydroxide (NaOH) dropwise to an 85 °C deoxygenated solution of $FeCl_3 \cdot 6H_2O$ followed by addition of a trace amount of $FeCl_2 \cdot 4H_2O$ ($n_{Fe(II)}/n_{Fe(III)} = 0.02$). The solution was refluxed in air for 4 hours. The precipitate was washed 5 times with ultrapure water and dried in a vacuum oven at 50 °C.

2.3.2 Suppliers. γ-Fe_2O_3 nanoparticles (<50 nm) and α-Fe_2O_3 nanoparticles were procured from Sigma-Aldrich and Alfa Aesar, respectively. The reagents for synthesis of Fe_3O_4 and α-FeOOH : NH_4OH (28.0–30.0% NH_3 weight basis, ACS reagent), NaOH (≥97.0%, ACS reagent), $FeCl_3 \cdot 6H_2O$ (≥97.0%, ACS reagent) and $FeCl_2 \cdot 4H_2O$ (≥98.0%), were purchased from Sigma-Aldrich and used without further purification.

Extra dry air (19.5% ≤ O_2 ≤ 23.5% and H_2O < 10 ppm), from Praxair, was used as the diluent to prepare gas phase solutions of Hg^0. 18.2 MΩ deionized water from a Milli-Q (Millipore) system was used to generate water vapor for experiments conducted with humidity.

3. Results and discussions

In this section, we report and discuss the physical and chemical characterization of the iron (oxyhydr)oxide particles, uptake coefficients, adsorption isotherms and the influence of humidity and irradiation on the uptake reactions. We subsequently integrate our observations to propose potential

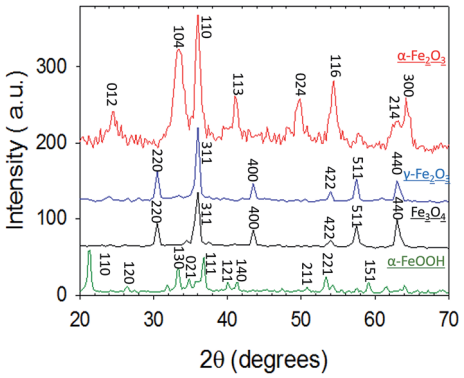

Fig. 1 X-Ray Diffraction (XRD) patterns of α-Fe_2O_3 (red), γ-Fe_2O_3 (blue), Fe_3O_4 (black) and α-FeOOH (green).

mechanisms for these reactions, and further conceptualize their implications for atmospheric Hg models.

3.1 Characterization of iron (oxyhydr)oxides

3.1.1 Iron (oxyhydr)oxide XRD analysis. The XRD pattern (Fig. 1) of magnetite ($FeO \cdot Fe_2O_3$) was matched to the standard reference JCPDS #19-069. Ferric oxide from Sigma Aldrich was found to be present primarily as maghemite (γ-Fe_2O_3), matching the standard reference JCPDS #39-1346 while ferric oxide from Alfa Aesar was found to be present predominantly as hematite (α-Fe_2O_3), matching JCPDS #86-0550. FeOOH was present as goethite (α-FeOOH) and matched to JCPDS #29-713. Within detection limits of the instrument, peaks of other crystalline impurities were not detected.

3.1.2 Iron (oxyhydr)oxide particle size distribution. Results of NTA and TEM (shown as insets) size characterization of the iron (oxyhydr)oxides is illustrated in Fig. 2. The hydrodynamic radii of aqueous suspensions of the iron (oxyhydr)oxides, obtained by averaging 6 runs per sample, is represented by the black trace with their weighted standard deviations shown in red. TEM images of Fe_3O_4 and γ-Fe_2O_3 showed that they were present as spheres and cuboids measuring 10–20 nm and 15–50 nm, respectively, while α-FeOOH and α-Fe_2O_3 exhibited rod like structures with widths of 5–30 nm and 5–20 nm, respectively. The size distributions obtained with NTA were larger than those determined *via* TEM likely because NTA measured the hydrodynamic radii of nanoparticle aggregates rather than the individual nanoparticles.

3.2 Uptake of $Hg^0_{(g)}$ on iron (oxyhydr)oxides

3.2.1 Effect of iron (oxyhydr)oxides on $Hg^0_{(g)}$ uptake in dark conditions. Prior to the addition of iron (oxyhydr)oxide surfaces, controls were performed in the dark with $Hg^0_{(g)}$ in dry air to quantify wall losses. The resulting pseudo first order rate constant was found to be $(1.31 \pm 0.12) \times 10^{-4}$ min^{-1}, corresponding to a *ca.* 5% loss of $Hg^0_{(g)}$ over a period of 300 minutes (data shown in Section S4 of the ESI†). The addition of 0.5 g L^{-1} of α-Fe_2O_3 and α-FeOOH yielded k values (Table 1) that were similar to the control reactions, within limits of experimental uncertainty. Uptake on γ-Fe_2O_3 was found to be slightly larger

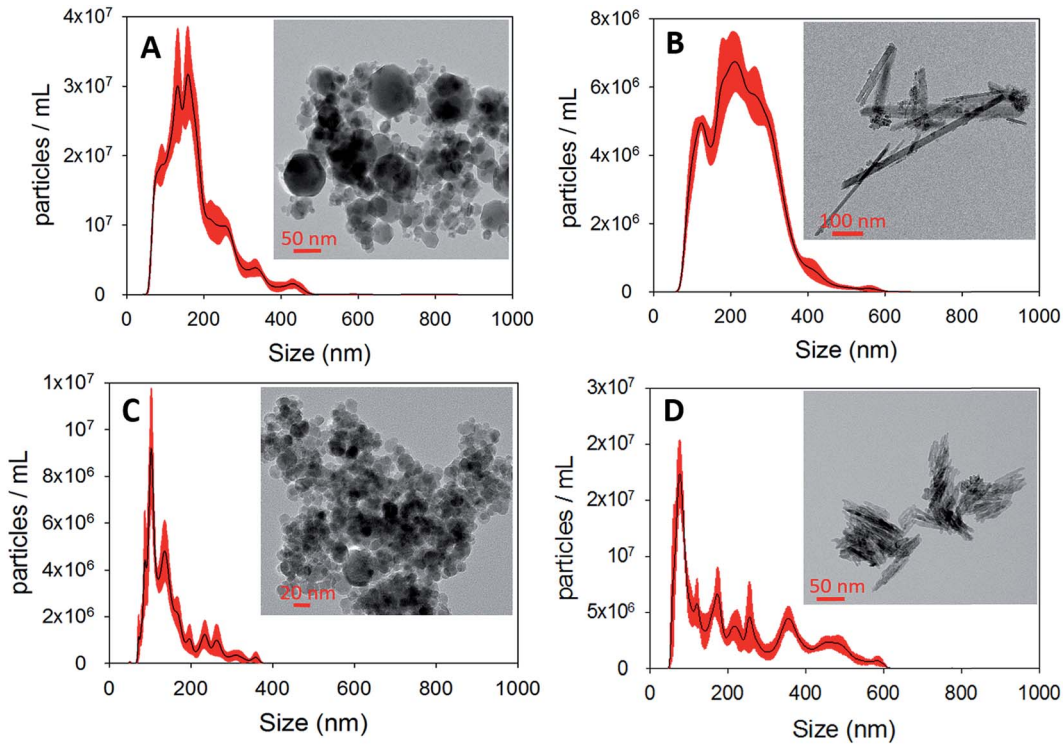

Fig. 2 NTA size distributions of (A) γ-Fe_2O_3 (B) α-FeOOH (C) Fe_3O_4 and (D) α-Fe_2O_3. The corresponding TEM micrographs are displayed as insets.

Table 1 Apparent pseudo first order rate constants (k) and uptake coefficients (γ) for the loss of $Hg^0_{(g)}$ on iron (oxyhydr)oxides (Fe_3O_4, α-FeOOH, γ-Fe_2O_3 and α-Fe_2O_3) under dark, UV-A, UV-B and visible light irradiation

		k [min^{-1}]	γ	$\gamma_{light}/\gamma_{dark}$
Fe_3O_4	Dark	$(1.15 \pm 0.17) \times 10^{-2}$	$(1.09 \pm 0.16) \times 10^{-10}$	1.00
	Visible	$(1.01 \pm 0.10) \times 10^{-2}$	$(9.66 \pm 0.95) \times 10^{-11}$	0.87
	UV-A	$(1.15 \pm 0.21) \times 10^{-2}$	$(1.09 \pm 0.20) \times 10^{-10}$	1.00
	UV-B	$(1.41 \pm 0.19) \times 10^{-2}$	$(1.35 \pm 0.18) \times 10^{-10}$	1.22
α-FeOOH	Dark	$(1.71 \pm 0.41) \times 10^{-4}$	$(2.11 \pm 0.51) \times 10^{-12}$	1.00
	Visible	$(1.87 \pm 0.58) \times 10^{-2}$	$(2.30 \pm 0.71) \times 10^{-10}$	109.35
	UV-A	$(1.62 \pm 0.12) \times 10^{-1}$	$(1.99 \pm 0.14) \times 10^{-9}$	947.36
	UV-B	$(9.67 \pm 2.08) \times 10^{-2}$	$(1.19 \pm 0.25) \times 10^{-9}$	565.49
γ-Fe_2O_3	Dark	$(9.50 \pm 0.71) \times 10^{-4}$	$(1.96 \pm 0.14) \times 10^{-11}$	1.00
	Visible	$(4.64 \pm 0.19) \times 10^{-2}$	$(9.57 \pm 0.39) \times 10^{-10}$	48.84
	UV-A	$(7.95 \pm 0.34) \times 10^{-2}$	$(1.64 \pm 0.70) \times 10^{-9}$	83.68
	UV-B	$(4.19 \pm 0.10) \times 10^{-2}$	$(8.64 \pm 0.21) \times 10^{-10}$	44.10
α-Fe_2O_3	Dark	$(3.70 \pm 2.12) \times 10^{-4}$	$(2.81 \pm 1.61) \times 10^{-12}$	1.00
	Visible	$(7.43 \pm 1.07) \times 10^{-2}$	$(5.64 \pm 0.81) \times 10^{-10}$	200.81
	UV-A	$(2.21 \pm 0.22) \times 10^{-1}$	$(1.59 \pm 0.16) \times 10^{-9}$	567.56
	UV-B	$(9.84 \pm 1.35) \times 10^{-2}$	$(7.47 \pm 1.03) \times 10^{-10}$	265.94

than $Hg^0_{(g)}$ wall loss, but, still of the same order as the control reactions. The highest uptakes were witnessed on the surface of Fe_3O_4, with a pseudo first order rate constant *ca.* 10^2 times greater than the wall loss.

3.2.2 Effect of irradiation on $Hg^0_{(g)}$ adsorption by iron (oxyhydr)oxides. Uptake reactions were then performed by irradiating the reaction chamber with visible, UV-A and UV-B radiation, separately. The reaction chamber was irradiated in successive pulses of 5, 10 and 15 minutes. Between each of the pulses, the iron (oxyhydr)oxide surfaces were aged in the dark. Temperature probes (Fischer Scientific), were placed on the outer wall of the reaction flask, to measure changes in temperatures across the different irradiation sources and pulse durations used in these experiments. The variations in temperatures were small ($\pm$0.2 °C) and were not expected to significantly interfere with the reaction kinetics. Additionally, control experiments (without iron (oxyhydr)oxides) in visible, UV-A, and UV-B radiation did not result in a measurable loss of $Hg^0_{(g)}$ (data shown in Section S5 of the ESI†).

3.2.2.1 Uptake of $Hg^0_{(g)}$ on γ-Fe_2O_3. Fig. 3A displays the loss of $Hg^0_{(g)}$ on γ-Fe_2O_3 with the different types of irradiation. The x-axis and y-axis depict the percentage loss of $Hg^0_{(g)}$ and time expressed in minutes, respectively. Grey bands represent periods of irradiation while the white spaces represent aging of the particles in the dark. It was observed that irradiation with visible, UV-A or UV-B radiation led to a rapid loss of $Hg^0_{(g)}$. t-Tests confirmed that $Hg^0_{(g)}$ concentrations after the irradiation pulses were statistically distinct from (a) $Hg^0_{(g)}$ concentrations prior to the pulse and (b) control reactions done in dark conditions. Since significant $Hg^0_{(g)}$ losses were not observed in (a) dark reactions with iron (oxyhydr) oxides and (b) irradiated controls without iron (oxyhydr) oxides, it was assumed that $Hg^0_{(g)}$ losses were driven by the irradiated γ-Fe_2O_3 surfaces. The loss of $Hg^0_{(g)}$ ceased with termination of each irradiation pulse, suggesting that aged γ-Fe_2O_3 surfaces were not involved in secondary reactions with $Hg^0_{(g)}$ post radiation exposure.

Continuous curves for the radiation driven loss of $Hg^0_{(g)}$ were obtained by splicing together changes in the concentration of $Hg^0_{(g)}$ over the 3 irradiation pulses. The spliced curves are shown in ESI, Section S6.† Pseudo first order rate constants for the loss of $Hg^0_{(g)}$ were obtained by fitting the data to the linearized form of the pseudo first order kinetic model. The model described the data well with $R^2 > 0.98$ for irradiated experiments. Dark reactions, however, were found to have low coefficients of determination ($R^2 < 0.52$) which were attributed to the changes in $Hg^0_{(g)}$ concentrations being similar to the instrumental variability ($\pm$10%).

The rate coefficients were normalized by the mass loading and BET surface area of γ-Fe_2O_3 to yield the uptake coefficients. It should be noted that using BET surface area, instead of geometric surface area, underestimates the values of γ as all the surfaces may not participate in the uptake reaction.[32] In real atmospheric and stack conditions iron (oxyhydr)oxides aerosols may be expected to be suspended in the air, increasing available surfaces for the uptake of $Hg^0_{(g)}$. We therefore regard our reported values of γ to be the lower bound estimates of these reactions.

The values of k and γ are summarized in Table 1. Under similar initial reaction conditions of $Hg^0_{(g)}$ and γ-Fe_2O_3 concentrations, temperature, humidity and reaction flask surface to volume ratio, γ values for irradiated experiments were *ca.* 40–80 times larger than dark reactions. The relative increase in γ was expressed as the ratio of the uptake coefficients on irradiation (γ_{light}) to the uptake coefficients of dark reactions (γ_{dark}), and presented in the last column of Table 1. It was additionally found that γ varied with the wavelength bands of radiation used. γ for the loss of $Hg^0_{(g)}$ was highest in UV-A > visible $\geq$ UV-B > dark. The dependence of γ on wavelength was suspected to be related to the optical properties of γ-Fe_2O_3, which were characterized with UV-Vis DRS.

Fig. 4 depicts a plot of the Kubelka–Munk function (top panel) and its first derivative (bottom panel) against wavelength (λ) of the iron (oxyhydr)oxides (the 250–800 nm spectra are

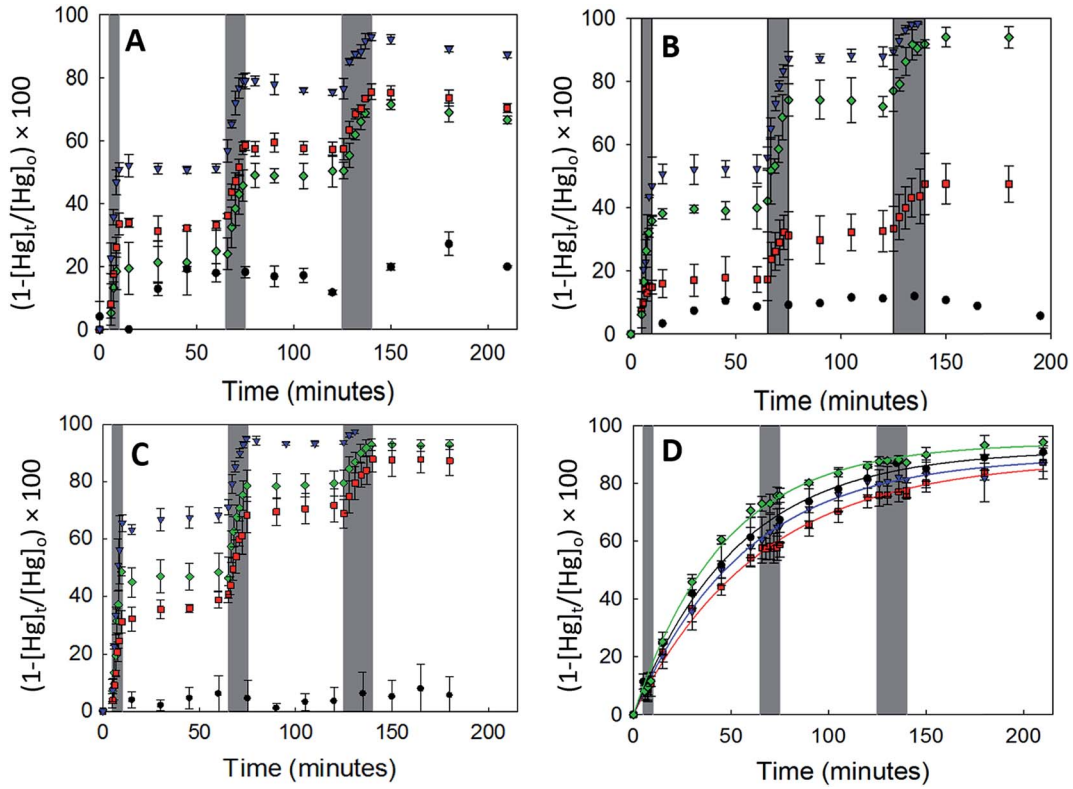

Fig. 3 Effect of dark (black circles), visible light (red squares), UV-A (blue inverted triangles) and UV-B (green diamonds) radiation on the uptake of Hg^0 by (A) γ-Fe_2O_3, (B) α-FeOOH, (C) α-Fe_2O_3 and (D) Fe_3O_4. Grey bands represent periods for which the irradiation sources were active. Error bars represent the standard deviation of 3 trials.

present in ESI, Section S7†). The band gaps calculated in this study are in agreement with previously published values.[33,34]

The band gap of γ-Fe_2O_3 was determined to be 2.39 eV (or 517 nm). Consequently, the entire UV-A band (315–400 nm), used in this study, was likely to have energies sufficient to promote electronic transitions in γ-Fe_2O_3. In contrast, electronic transitions due to visible radiation (400–700 nm) may have occurred only for $\lambda < 517$ nm. For $\lambda > 517$ nm, the incoming radiation was likely not energetically sufficient to promote transitions. As consequence of this only about 40–50% of the total impinged visible radiation may have excited electrons across the band gap, causing γ values to be lower with visible radiation than UV-A radiation. It is additionally possible that since electronic transitions in visible radiation arise from weaker indirect d–d transitions, compared to direct transitions in UV radiation,[35,36] the associated reactions kinetics are lower than those for direct transitions.[36]

Following the previous discussion, it was expected that the entire UV-B band (280–315 nm) had sufficient energy to promote electronic transitions and therefore result in uptake coefficients similar to those obtained with UV-A radiation. γ values for UV-B radiation were, however, seen to be only about ~50% of the γ values obtained with UV-A radiation. This apparent discrepancy was explained by the attenuation of UV-B radiation by the reaction chamber walls. The construction material of our reaction chambers – Pyrex (borosilicate glass)- is known to absorb UV-B radiation.[37] The radiation transmitted through the reaction chamber walls, characterized with a PM100A power meter (Thor Labs), was attenuated by ~53%, (characterization of radiation attenuation is presented in Section S2, Table S2 of the ESI†) thereby limiting its availability for the photolytic uptake of $Hg^0_{(g)}$.

3.2.2.2 Uptake of $Hg^0_{(g)}$ on α-Fe_2O_3 and α-FeOOH. To further explore the correlation between iron oxide band gaps and

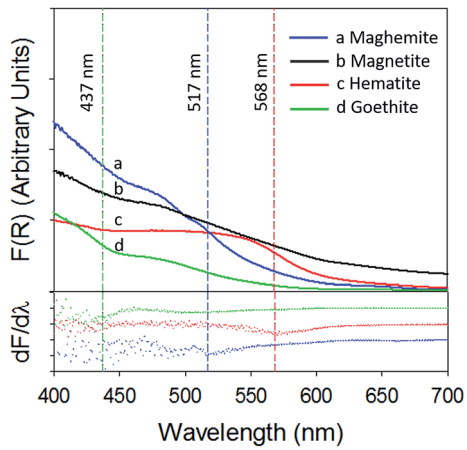

Fig. 4 Kubelka–Munk function (top panel) and its first derivative (bottom panel) of (a) γ-Fe_2O_3 (blue) (b) Fe_3O_4 (black) (c) α-Fe_2O_3 (red) and (d) α-FeOOH (green).

$Hg^0_{(g)}$ loss kinetics, $Hg^0_{(g)}$ uptake experiments, in dry air, were conducted with the additional iron oxides (α-Fe_2O_3, Fe_3O_4) and iron oxide-hydroxide (α-FeOOH).

α-Fe_2O_3 displayed similar adsorption characteristics as γ-Fe_2O_3, with enhanced $Hg^0_{(g)}$ loss kinetics (Fig. 3C) upon irradiation, under our experimental conditions. The enhancement of uptake kinetics in visible light was lower than that of UV-A radiation (Table 1). This is in agreement with (a) the calculated band gap of 568 nm (Table 2) for α-Fe_2O_3, because of which half the visible band was expected to lack sufficient energy to promote transitions between the valence and conduction bands and (b) the promotion of weaker indirect d–d transitions with visible radiation compared to stronger direct transitions with UV radiation, as discussed before.[36]

Similar to our observations for γ-Fe_2O_3 and α-Fe_2O_3, we observed the loss of $Hg^0_{(g)}$ on α-FeOOH when irradiated (Fig. 3B). However, in contrast to γ-Fe_2O_3 and α-Fe_2O_3, the activity in the visible region was only about 11.5% of that observed in UV-A irradiation experiments (Table 1). The calculated band gap for α-FeOOH was found to be 437 nm, which likely limited the spectrum of the visible region, capable of causing transitions, to 12% (400–437 nm) of the 400–700 nm visible band. It has been shown that for α-FeOOH the energies of direct band transitions decrease from 3.2 eV ($\lambda = 387$ nm) to a limiting value of 2.5 eV ($\lambda = 495$ nm), and energies of indirect transitions decrease from 2.1–1.6 eV ($\lambda = 590$–774 nm) with increasing particle size from 8 nm to 40 nm.[38] Therefore it can be expected that size is a crucial factor in determining $Hg^0_{(g)}$ loss on irradiated α-FeOOH.

It should be noted that the maximum uptake kinetics for $Hg^0_{(g)}$ loss on α-Fe_2O_3 and α-FeOOH were observed with UV-A illumination. The increase in γ values were large; approximately 567 and 947-fold greater than dark reactions on the surfaces of α-Fe_2O_3 and α-FeOOH, respectively.

It was also observed that rate of loss of $Hg^0_{(g)}$ on α-Fe_2O_3 and α-FeOOH in the presence of UV-B was, within limits of experimental uncertainty, half that of UV-A. This was attributed to the attenuation of UV-B radiation transmitted through the reaction chamber walls, as discussed before.

3.2.2.3 Uptake of $Hg^0_{(g)}$ on Fe_3O_4. With Fe_3O_4, $Hg^0_{(g)}$ losses were observed in the dark. Illumination with UV and visible radiation did not yield measurable changes in $Hg^0_{(g)}$ loss kinetics relative to the dark reactions (Fig. 3D). Fe_3O_4 absorbed at all wavelengths examined in this study using UV-Vis DRS (ESI, Section S7†). No clear peaks were observed in the first derivative plot of Fe_3O_4 and it was therefore omitted from Fig. 4 to improve clarity. The mechanisms of the photolytic uptake of $Hg^0_{(g)}$ on α-Fe_2O_3, α-FeOOH and γ-Fe_2O_3, and the reasons for the lack of photolytic activity on the surface of Fe_3O_4 are discussed in Section 3.6.

Table 2 Calculated values of band gaps and specific surface areas of the iron (oxyhydr)oxides (Fe_3O_4, α-FeOOH, γ-Fe_2O_3 and α-Fe_2O_3) used in this study

Iron oxide	Band gap (eV)	Specific surface area ($m^2\ g^{-1}$)
Fe_3O_4	—	72.85 ± 0.63
α-FeOOH	2.83	56.51 ± 1.52
γ-Fe_2O_3	2.39	33.78 ± 1.48
α-Fe_2O_3	2.18	91.71 ± 0.35

3.3 Effect of concentration on uptake kinetics and uptake coefficient

To study the dependence of γ on the mass loading of the iron oxides, adsorption experiments were done with varying concentrations of α-Fe_2O_3 (0.013 g L^{-1} to 0.613 g L^{-1}) in visible light (Fig. 5A). On visual inspection, the coating was sparse for α-Fe_2O_3 concentration of 0.013 g L^{-1}, yet increased steadily with increasing concentration up to 0.272 g L^{-1}. At concentrations >0.272 g L^{-1} the coating appeared densest with excess α-Fe_2O_3 accumulating at the bottom of the reaction chamber.

The calculated values of k and γ are shown in Fig. 5B. It was observed that k increased almost linearly with increasing concentrations of α-Fe_2O_3 from 0.013 g L^{-1} to 0.272 g L^{-1}, however, a further increase in concentrations from 0.272 g L^{-1} to 0.613 g L^{-1} did not lead to a corresponding increase in k.

This stabilization of k was attributed to the non-participation of additional surfaces beyond a concentration of 0.272 g L^{-1}. Since the adsorption process was photolytic, we expected only irradiated iron oxide surfaces to participate in the reaction. From reported penetration depths of radiation through α-Fe_2O_3 (118 nm at $\lambda = 550$ nm),[39] light may be expected to travel only through a few monolayers of the α-Fe_2O_3 nanoparticle coating

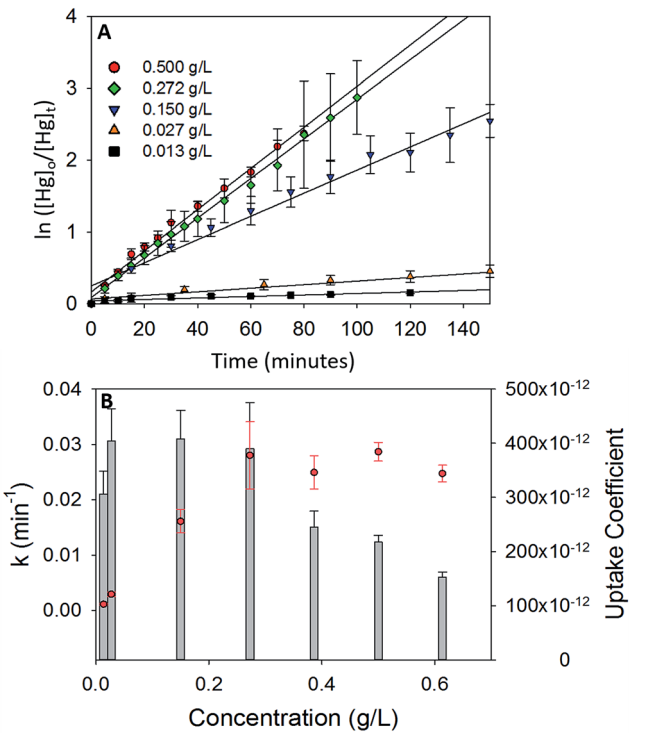

Fig. 5 (A) Pseudo first order plots for $Hg^0_{(g)}$ loss on different concentrations of α-Fe_2O_3 in visible light. (B) Variation of pseudo first order rate constant (k, red circles) and uptake coefficients (γ, grey bar graphs) with concentration of α-Fe_2O_3.

before being extinguished. Increases in mass loadings of α-Fe_2O_3, beyond 0.272 g L^{-1}, presumably inhibited radiation from reaching α-Fe_2O_3 particles that were (a) further away from the illuminated surfaces and (b) accumulated at the bottom of the chamber. Since these additional surfaces were not irradiated, they were expected to not contribute to the photolytic uptake of $Hg^0_{(g)}$ thereby limiting k values. Stabilization of k values was reflected in further underestimation of the uptake coefficients. While γ was similar for α-Fe_2O_3 loadings of 0.027–0.272 g L^{-1}, it decreased on increasing α-Fe_2O_3 loading beyond 0.272 g L^{-1}. This trend was explained *via* eqn (E3). Above concentrations of 0.272 g L^{-1}, k values remained constant, while C_{mass} increased, leading to decreases in the calculated values of γ.

It was additionally observed that for the adsorption of $Hg^0_{(g)}$ on α-Fe_2O_3 in visible light, γ values averaged over 3 trials were lower for experiments done in 5.5 L chambers ($\gamma = (3.90 \pm 0.59) \times 10^{-10}$) than 2.0 L chambers ($\gamma = (5.64 \pm 0.81) \times 10^{-10}$). The difference was proportional to the difference in the surface to volume (S/V) ratios of the reaction chambers ($(S/V)_{5.5\ L}/(S/V)_{2.0\ L} = 0.717$ and $\gamma_{5.5\ L}/\gamma_{2.0\ L} = 0.709$). The increase in uptake kinetics with S/V ratios of the reaction chambers was likely due to the larger abundance of iron oxide surfaces on the walls of the reaction chamber, relative to the bulk, that participated in the photolytic uptake of $Hg^0_{(g)}$.

3.4 Effect of water vapor on uptake coefficient

The values of γ discussed so far have only dealt with the adsorption of $Hg^0_{(g)}$ on the iron oxides in dry conditions. However, such conditions are unlikely in atmosphere due to the relative abundance of water vapor. To address the influence of water vapor, uptake reactions on α-Fe_2O_3 were performed at relative humidities of <1%, 33%, 66% and 95%, in the presence of visible and UV-A radiation. We opted to exclude supersaturation conditions to avoid secondary reactions (*e.g.*, solid/aqueous condensed phase chemistry), which occurs close to or over saturation point.

The reaction variables and uptake coefficients are summarized in Table 3. It was observed that γ decreased rapidly with increasing relative humidity. Even at the low relative humidity of 33%, γ decreased by 89% and 93% for visible radiation and UV-A radiation, respectively, relative to the dry reactions.

The decrease in the uptake kinetics was attributed to competitive adsorption between water molecules and $Hg^0_{(g)}$ atoms for active sites on α-Fe_2O_3's surface. As shown in previous research, the introduction of water vapor at increasing relative humidity, results in further water uptake by hematite.[16] Once adsorbed, water molecules may have inhibited contact between the surface sites and $Hg^0_{(g)}$ atoms, thereby preventing its photolytic uptake. It should be noted that a previous study with a flow through system at elevated temperatures studied the effect of humidity, but not radiation, on $Hg^0_{(g)}$ adsorption by α-Fe_2O_3. They reported that while water vapor concentrations of up to 2% promoted $Hg^0_{(g)}$ uptake, concentrations above 2% inhibited $Hg^0_{(g)}$ adsorption.[40]

3.5 Adsorption isotherm

The Langmuir, Freundlich and Elovich models used in this study represent different physical basis for adsorption.

3.5.1 Langmuir adsorption isotherm. The Langmuir adsorption isotherm is a theoretical model that assumes homogeneous adsorption sites and mono-layer coverage. The linear form of the Langmuir adsorption isotherm is represented by:

$$\frac{C_e}{q_e} = \frac{1}{Q_m K_L} + \frac{C_e}{Q_m} \quad \text{(E4)}$$

where C_e is the equilibrium concentration of Hg^0 ($\mu g\ L^{-1}$) and q_e is the amount of Hg^0 adsorbed per gram of α-Fe_2O_3. The maximum adsorption capacity (Q_m) is obtained from the slope of the linear fit of C_e/q_e against C_e and the Langmuir isotherm constant (K_L) is obtained from the intercept.

The separation factor (R_L) is defined as:

$$R_L = \frac{1}{1 + K_L C_o} \quad \text{(E5)}$$

where C_o is the initial Hg^0 concentration ($\mu g\ L^{-1}$).

3.5.2 Freundlich adsorption isotherm. The Freundlich adsorption isotherm is an empirical fit that allows for heterogeneous adsorption sites.

$$\log(q_e) = \log(K_F) + \frac{1}{n}\log(C_e) \quad \text{(E6)}$$

A linear fit of $\log(q_e)$ *vs.* $\log(C_e)$ yields the adsorption intensity (n) and the Freundlich adsorption isotherm constant (K_F). The

Table 3 Apparent pseudo first order rate constants (k) and uptake coefficients (γ) for the loss of $Hg^0_{(g)}$ on α-Fe_2O_3 in visible light and UV-A with 0% < RH < 100%

Effect of humidity on the uptake coefficient							
S. no.	Conc. (g L^{-1})	RH (%)	Radiation	k (min^{-1})	γ	$\gamma_{wet}/\gamma_{dry}$	$\gamma_{light}/\gamma_{dark}$
1	0.272	0	Visible	$(2.81 \pm 0.61) \times 10^{-2}$	$(3.90 \pm 0.59) \times 10^{-10}$	1.00	142.21
2	0.272	33	Visible	$(0.33 \pm 0.03) \times 10^{-2}$	$(0.46 \pm 0.04) \times 10^{-10}$	0.11	16.35
3	0.272	66	Visible	$(0.16 \pm 0.01) \times 10^{-2}$	$(0.22 \pm 0.01) \times 10^{-10}$	0.05	7.93
4	0.272	95	Visible	$(0.12 \pm 0.03) \times 10^{-2}$	$(0.17 \pm 0.04) \times 10^{-10}$	0.04	5.94
5	0.272	0	UV-A	$(3.20 \pm 0.40) \times 10^{-2}$	$(4.46 \pm 0.41) \times 10^{-10}$	1.00	158.56
6	0.272	33	UV-A	$(0.24 \pm 0.02) \times 10^{-2}$	$(0.33 \pm 0.03) \times 10^{-10}$	0.07	11.89
7	0.272	66	UV-A	$(0.16 \pm 0.01) \times 10^{-2}$	$(0.22 \pm 0.01) \times 10^{-10}$	0.05	7.92
8	0.272	95	UV-A	$(0.06 \pm 0.01) \times 10^{-2}$	$(0.08 \pm 0.01) \times 10^{-10}$	0.02	2.84

adsorption capacity (Q_m) is obtained by replacing C_e by the initial $Hg^0_{(g)}$ concentration (C_o), in eqn (E6).[41]

3.5.3 Elovich adsorption isotherm.

$$\ln\left(\frac{q_e}{C_e}\right) = -\frac{q_e}{Q_m} + \ln(K_E Q_m) \quad \text{(E7)}$$

The Elovich adsorption isotherm represents multilayer adsorption. The maximum adsorption capacity (Q_m) and Elovich adsorption isotherm constant (K_E) were obtained from the slope and intercept, respectively, of the linear fit of $\ln(q_e/C_e)$ to q_e.

3.5.4 Comparison of the adsorption isotherms. The linearized forms of the adsorption isotherms were fit to the experimental data. On the basis of the coefficient of determination (Table 4) the Langmuir isotherm (Fig. 6) was found to fit the data most closely ($R^2 > 0.99$), followed by the Freundlich and Elovich adsorption isotherms. Monolayer coverage, demonstrated by the fit of the Langmuir adsorption isotherm, is consistent with the possibility of oxidized Hg blocking active sites on α-Fe_2O_3, preventing further photolytic uptake of $Hg^0_{(g)}$.

The favorability of adsorption for the Langmuir and Freundlich adsorption isotherms are decided based on the separation factor (R_L) and adsorption intensity (n) respectively. R_L and n are characteristic of the adsorbent–adsorbate system. Adsorption is said to be favorable if $0 < R_L < 1$ and $1/n < 1$ (or $n > 1$). The computed values of R_L (0.02) and n (8.77) suggest that $Hg^0_{(g)}$ adsorption onto α-Fe_2O_3 in the presence of visible light is highly favorable. The adsorption capacities of Hg on α-Fe_2O_3 were similar for the Langmuir and Freundlich models, yielding a maximum adsorption capacity of (127.23 ± 2.23) μg g^{-1}.

3.6 Potential adsorption mechanism

Previous studies on the photolytic uptake of $Hg^0_{(g)}$ by TiO_2 have suggested electronic excitation from the Conductance Band (CB) to the Valence Band (VB) leads to superoxide and hydroxyl radical formation.[42] The hydroxyl radicals have been proposed to react with Hg^0 oxidizing it on the surface of TiO_2. For γ-Fe_2O_3, α-Fe_2O_3 and α-FeOOH, the strong correlation of irradiation with $Hg^0_{(g)}$ uptake considered in tandem with their band structure hints at similarities in the uptake mechanisms. Excitation to the CBs, from upper levels of the VBs are responsible for their respective optical absorption edges.[43] The oxidation potential of the holes (h^+) > +2.27 eV is sufficient to potentially generate hydroxyl radicals from surface water (Fig. 7A), which may then oxidize Hg^0. Evidence for the formation of hydroxyl radicals on the surfaces of γ-Fe_2O_3, α-Fe_2O_3 and α-FeOOH surfaces have previously been reported.[44–46]

The lack of radiation effects on uptake of Hg^0 on magnetite surfaces maybe explained by Fe_3O_4's low band gap value (~0.1 eV).[33] Consequently, the oxidation potential of the holes (Fig. 7) generated is insufficient to produce the hydroxyl radicals required to oxidize Hg^0.

Thermodynamic studies have suggested that direct HgO formation from the reaction of Hg^0 and $^{\bullet}OH$ is endothermic (ΔH = +90 kJ mol^{-1}), while HgO formation in the pathway involving O_2 is exothermic (ΔH = −118 kJ mol^{-1}).[48] We thus suspect that surface hydroxyls oxidized Hg^0 to HgO *via* formation of an intermediate Hg–$^{\bullet}OH$ complex, which then reacted with molecular oxygen.

The reduction potential of γ-Fe_2O_3 CB electrons may favor the 2 e^- reduction of oxygen to peroxides along with the formation of superoxides as reported for TiO_2.[42] The overall oxidation pathway, consistent with previously suggested mechanisms of iron oxide photo activity,[49–51] may be represented by reactions R1–R6, yet due to the complexity of pathways for such reactions on iron (oxyhydr)oxide surfaces[49,51–53] further experimental investigation on the precise mechanism is encouraged.

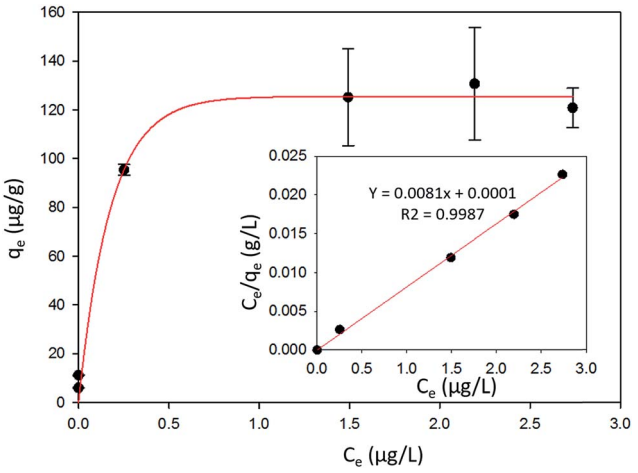

Fig. 6 The amount of Hg^0 adsorbed per unit mass of α-Fe_2O_3 (q_e) *vs.* the gas phase concentration of Hg^0 (C_e) at equilibrium. The inset shows the fit to the linearized form of the Langmuir adsorption isotherm.

Table 4 Calculated values of fitting parameters and coefficient of determination (R^2) for the fit of Langmuir, Freundlich and Elovich adsorption models to experimental data

Model	Parameters			
Langmuir	Q_m (μg g^{-1})	K_L (L μg^{-1})	R_L	R^2
	125.00	20	0.02	0.99
Freundlich	Q_m (μg g^{-1})	K_F (μg g^{-1}) (L $g^{-1})^n$	n	R^2
	129.47	113.35	8.77	0.88
Elovich	Q_m (μg g^{-1})	K_E (L μg^{-1})	N.A.	R^2
	16.23	7730.32	N.A.	0.84

$$Fe_2O_3 + h\nu \rightarrow e^- + h^+ \quad \text{(R1)}$$

$$H_2O + h^+ \rightarrow OH^{\bullet} + H^+ \quad \text{(R2)}$$

$$O_2 + 2e^- + 2H^+ \rightarrow H_2O_2 \quad \text{(R3)}$$

$$H_2O_2 + e^- \rightarrow OH^{\bullet} + {-}OH \quad \text{(R4)}$$

$$Hg^0 + OH^{\bullet} \rightarrow {}^{\bullet}HgOH\ (+M) \quad \text{(R5)}$$

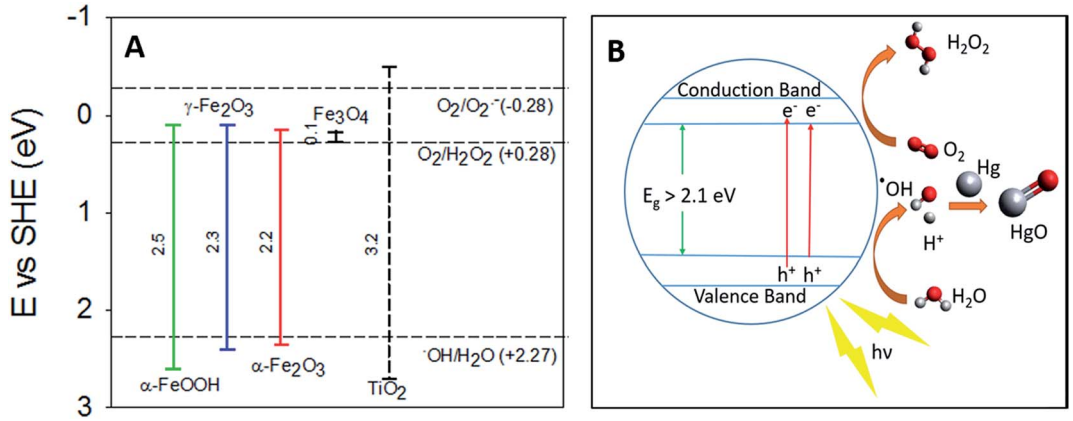

Fig. 7 (A) Band gaps of TiO_2, α-FeOOH, α-Fe_2O_3 and γ-Fe_2O_3 compared with redox potentials of hydroxyl, peroxide and superoxide radicals (the redox potentials described here are compiled from the work of Liu,[33] Fujishima *et al.*,[47] and Sherman[34]). (B) Graphical representation of proposed radiation enhanced $Hg^0_{(g)}$ loss mechanism.

$$^{\bullet}HgOH + O_2 \rightarrow \textit{via}\ \text{intermdiates/surfaces} \rightarrow HgO(s) + HO_2^{\bullet} \quad (R6)$$

For convenience, the simplified reaction scheme is depicted in Fig. 7B.

Spent iron (oxyhydr)oxides were characterized with X-ray Photon Spectroscopy (XPS) and Energy Dispersive Analysis of X-ray (EDAX) to identify post reaction Hg speciation. We were unable to detect Hg because its surface concentrations ($\approx$120 μg g^{-1}) were lower than the working detection limit of the instruments ($\approx$0.05% or 500 μg g^{-1}).

Additionally, to check for the temperature dependent reversibility of Hg binding on α-Fe_2O_3, which could potentially affect the release of Hg in warmer climates, the reaction chamber, post reaction, was heated from 23 °C to 150 °C in an oil bath. Hg desorption was not detected up to 100 °C, however, at 110 °C Hg release back into the gas phase was observed. The maximum $Hg^0_{(g)}$ released was *ca.* 10% of the initial concentration at 120 °C. $Hg^0_{(g)}$ concentrations did not increase significantly on increasing the temperature to 150 °C or prolonged heating (65 minutes at 150 °C). Re-volatilization of those Hg^0 atoms that were weakly adsorbed on the chamber walls (*ca.* 5%, as reported before) and α-Fe_2O_3 surfaces were likely responsible for the observed Hg signals. Since tropospheric temperatures are lower than the temperatures reported here, we expect that temperature alone will not affect the release of Hg bound to α-Fe_2O_3 particles in warmer climates. It is, however, possible that other atmospheric species such as water vapor and organic species such as BTEX in conjunction with temperature may affect α-Fe_2O_3 bound Hg differently. Such interactions are yet to be studied.

Although the focus of our studies was to understand the reactions of elemental mercury with ubiquitous dust particles and the effect of photochemical aging and the humidity on the particles, such nanoparticles can also be used for mercury remediation. There is already a wide range of promising natural[42] and synthetic[54,55] materials in literature and further investigation into exploiting the photoactivity of iron (oxyhydr)oxides for remediation processes is encouraged.

4. Conclusions and future work

In this study, we provided evidence for the uptake of $Hg^0_{(g)}$ on the surfaces iron (oxyhydr)oxide particles. The uptake of $Hg^0_{(g)}$ on α-FeOOH, γ-Fe_2O_3 and α-Fe_2O_3, was found to be significantly influenced by UV-visible radiation. In dark conditions, uptake of $Hg^0_{(g)}$ on these iron oxides were comparable to wall losses, suggesting limited uptake of $Hg^0_{(g)}$. Despite the inhibition of uptake reactions on α-Fe_2O_3 by humidity, γ values for these reactions (at RH $\leq$ 66%) were higher than γ values for $Hg^0_{(g)}$ losses in dark. Additionally, while $Hg^0_{(g)}$ uptake on the surfaces of α-FeOOH, γ-Fe_2O_3 and α-Fe_2O_3 were driven by UV-visible radiation, the uptake of $Hg^0_{(g)}$ on Fe_3O_4 was not. The difference in uptake behavior of the iron (oxyhydr)oxides were attributed to their band gaps and consequently the redox potentials of the electron–hole pairs. It is important to note that while only 4 iron (oxyhydr)oxides were investigated in this study, we believe that other oxides and hydroxides of metals (such as manganese) with suitable band gaps may also be active in the photolytic capture of $Hg^0_{(g)}$. This can potentially increase the number of chemical pathways available for the formation of PBM and deposition of $Hg^0_{(g)}$, however, further studies are required to identify and characterize such reactions.

Mercury models are used to assess the impact of changes in anthropogenic mercury emissions such as expected under the Minamata convention on mercury levels in environmental ecosystems; however, accurate representation of mercury chemistry in models remains a challenge. The long-range transport of mercury and its impact on global ecosystems are largely determined by the physicochemical processes involved in the removal of Hg^0 from the atmosphere. Uptake of $Hg^0_{(g)}$ on particulate matter in air and at terrestrial surfaces could explain a significant pathway for the deposition of Hg^0. This study provides insights into the mechanism for gas-particle partitioning of Hg^0 for selected ambient aerosol surfaces under

various environmental conditions. Further studies are required to fully determine the mechanism involved in gas-particle interactions of Hg^0 for different heterogeneous surfaces in the biosphere, and modeling studies are needed to investigate the impact of these processes on the lifetime of mercury in the atmosphere.

Conflicts of interest

There are no conflicts of interest to declare.

Appendix

γ	Uptake coefficient
λ	Wavelength (nm)
ν_{Hg}	Mean molecular velocity of $Hg^0_{(g)}$ at 22.3 °C (m min^{-1})
C_{mass}	Mass loading of sorbent in reaction chamber (g m^{-3})
$[C]_e$	Equilibrium concentration of $Hg^0_{(g)}$ (μg L^{-1})
$F(R)$	Kubelka–Munk function
$[Hg]_o$	Concentration of $Hg^0_{(g)}$ at time $t = 0$ (μg L^{-1})
$[Hg]_t$	Concentration of $Hg^0_{(g)}$ at time t (μg L^{-1})
k	Pseudo-first order rate constant (min^{-1})
K_E	Elovich isotherm constant (L μg^{-1})
K_F	Freundlich isotherm constant (μg g^{-1}) (L $g^{-1})^n$
K_L	Langmuir isotherm constant (L μg^{-1})
n	Adsorption intensity
q_e	Equilibrium concentration of Hg^0 on sorbent (μg g^{-1})
Q_m	Maximum adsorption capacity of sorbent (μg g^{-1})
R^2	Coefficient of determination
R	Reflectance
R_L	Separation factor
S_{BET}	BET surface area of the sorbent (m^2 g^{-1})
t	Time (minutes)
T	Temperature (°C)

Acknowledgements

This study was supported by funding from Environment and Climate Change Canada. We are also grateful to NSERC and NSERC-CREATE Mines of Knowledge for partial financial support.

References

1 C. Seigneur, K. Vijayaraghavan, K. Lohman, P. Karamchandani and C. Scott, *Environ. Sci. Technol.*, 2004, **38**, 555–569.
2 C. T. Driscoll, R. P. Mason, H. M. Chan, D. J. Jacob and N. Pirrone, *Environ. Sci. Technol.*, 2013, **47**, 4967–4983.
3 F. M. M. Morel, A. M. L. Kraepiel and M. Amyot, *Annu. Rev. Ecol. Syst.*, 1998, **29**, 543–566.
4 P. B. Tchounwou, W. K. Ayensu, N. Ninashvili and D. Sutton, *Environ. Toxicol.*, 2003, **18**, 149–175.
5 AMAP/UNEP, 2013. Technical Background Report for the Global Mercury Assessment 2013. Arctic Monitoring and Assessment Programme, Oslo, Norway/UNEP Chemicals Branch, Geneva, Switzerland. vi + 263 pp.
6 L. Zhang, P. Blanchard, D. Gay, E. Prestbo, M. Risch, D. Johnson, J. Narayan, R. Zsolway, T. Holsen and E. Miller, *Atmos. Chem. Phys.*, 2012, **12**, 4327–4340.
7 L. Zhang, P. Blanchard, D. Johnson, A. Dastoor, A. Ryzhkov, C. J. Lin, K. Vijayaraghavan, D. Gay, T. M. Holsen, J. Huang, J. A. Graydon, V. L. St Louis, M. S. Castro, E. K. Miller, F. Marsik, J. Lu, L. Poissant, M. Pilote and K. M. Zhang, *Environ. Pollut.*, 2012, **161**, 272–283.
8 A. J. Hynes, D. L. Donohoue, M. E. Goodsite and I. M. Hedgecock, in *Mercury Fate and Transport in the Global Atmosphere*, Springer, 2009, pp. 427–457.
9 J. J. Tokos, B. o. Hall, J. A. Calhoun and E. M. Prestbo, *Atmos. Environ.*, 1998, **32**, 823–827.
10 H. A. Wiatrowski, S. Das, R. Kukkadapu, E. S. Ilton, T. Barkay and N. Yee, *Environ. Sci. Technol.*, 2009, **43**, 5307–5313.
11 P. R. Kim, Y. J. Han, T. M. Holsen and S. M. Yi, *Atmos. Environ.*, 2012, **61**, 94–102.
12 M. Subir, P. A. Ariya and A. P. Dastoor, *Atmos. Environ.*, 2012, **46**, 1–10.
13 P. Ariya, J. Sun, N. Eltouny, E. Hudson, C. Hayes and G. Kos, *Int. Rev. Phys. Chem.*, 2009, **28**, 1–32.
14 C. R. Usher, A. E. Michel and V. H. Grassian, *Chem. Rev.*, 2003, **103**, 4883–4940.
15 E. Journet, K. V. Desboeufs, S. Caquineau and J. L. Colin, *Geophys. Res. Lett.*, 2008, **35**, L07805.
16 P. K. Mogili, P. D. Kleiber, M. A. Young and V. H. Grassian, *J. Phys. Chem. A*, 2006, **110**, 13799–13807.
17 Y. Dupart, S. M. King, B. Nekat, A. Nowak, A. Wiedensohler, H. Herrmann, G. David, B. Thomas, A. Miffre, P. Rairoux, B. D'Anna and C. George, *Proc. Natl. Acad. Sci. U. S. A.*, 2012, **109**, 20842–20847.
18 M. Ndour, M. Nicolas, B. D'Anna, O. Ka and C. George, *Phys. Chem. Chem. Phys.*, 2009, **11**, 1312–1319.
19 H. Zhang, *Recent Developments in Mercury Science*, 2006, pp. 37–79.
20 R. Bhardwaj, X. Chen and R. D. Vidic, *J. Air Waste Manage. Assoc.*, 2009, **59**, 1331–1338.
21 J.-E. Jung, D. Geatches, K. Lee, S. Aboud, G. E. Brown and J. Wilcox, *J. Phys. Chem. C*, 2015, **119**, 26512–26518.
22 T. Liu, L. Xue, X. Guo, J. Liu, Y. Huang and C. Zheng, *Environ. Sci. Technol.*, 2016, **50**(24), 13585–13591.
23 S. Lafon, I. N. Sokolik, J. L. Rajot, S. Caquineau and A. Gaudichet, *J. Geophys. Res.: Atmos.*, 2006, **111**, D21207.
24 B. Gilbert, C. Frandsen, E. R. Maxey and D. M. Sherman, *Phys. Rev. B: Condens. Matter Mater. Phys.*, 2009, **79**, 035108.
25 G. Snider, F. Raofie and P. A. Ariya, *Phys. Chem. Chem. Phys.*, 2008, **10**, 5616–5623.
26 A. Bouzaza and A. Laplanche, *J. Photochem. Photobiol., A*, 2002, **150**, 207–212.
27 J. Li, N. Yan, Z. Qu, S. Qiao, S. Yang, Y. Guo, P. Liu and J. Jia, *Environ. Sci. Technol.*, 2009, **44**, 426–431.
28 J. H. Sienfeld and S. N. Pandis, *Atmospheric Chemistry and Physics: From Air Pollution to Climate Change*, J. Wiley, New York, 1st edn, 1998.
29 A. R. Ravishankara, *Science*, 1997, **276**, 1058–1065.

30 P. K. Mogili, P. D. Kleiber, M. A. Young and V. H. Grassian, *J. Phys. Chem. A*, 2006, **110**, 13799–13807.
31 R. Massart, *IEEE Trans. Magn.*, 1981, **17**, 1247–1248.
32 J. Adams, D. Rodriguez and R. Cox, *Atmos. Chem. Phys.*, 2005, **5**, 2679–2689.
33 S. Q. Liu, *Environ. Chem. Lett.*, 2012, **10**, 209–216.
34 D. M. Sherman, *Geochim. Cosmochim. Acta*, 2005, **69**, 3249–3255.
35 M. F. Silva, L. A. de Oliveira, M. A. Ciciliati, L. T. Silva, B. S. Pereira, A. A. W. Hechenleitner, D. M. Oliveira, K. R. Pirota, F. F. Ivashita and A. Paesano Jr, *J. Appl. Phys.*, 2013, **114**, 104311.
36 T. K. Townsend, E. M. Sabio, N. D. Browning and F. E. Osterloh, *Energy Environ. Sci.*, 2011, **4**, 4270–4275.
37 D. E. Moore, in *Photostability of drugs and drug formulations*, ed. H. H. Tonnesen, CRC Press, Boca Raton, 2nd edn, 2004, ch. 2, pp. 9–37.
38 H. Z. Zhang, M. Bayne, S. Fernando, B. Legg, M. Q. Zhu, R. L. Penn and J. F. Banfield, *J. Phys. Chem. C*, 2011, **115**, 17704–17710.
39 A. G. Tamirat, J. Rick, A. A. Dubale, W.-N. Su and B.-J. Hwang, *Nanoscale Horiz.*, 2016, **1**, 243–267.
40 F. Kong, J. Qiu, H. Liu, R. Zhao and Z. Ai, *J. Environ. Sci.*, 2011, **23**, 699–704.
41 O. Hamdaoui and E. Naffrechoux, *J. Hazard. Mater.*, 2007, **147**, 381–394.
42 G. Snider and P. Ariya, *Chem. Phys. Lett.*, 2010, **491**, 23–28.
43 R. Grau-Crespo, A. Y. Al-Baitai, I. Saadoune and N. H. De Leeuw, *J. Phys.: Condens. Matter*, 2010, **22**, 255401.
44 P. Mazellier and M. Bolte, *J. Photochem. Photobiol., A*, 2000, **132**, 129–135.
45 B. Ahmmad, K. Leonard, M. S. Islam, J. Kurawaki, M. Muruganandham, T. Ohkubo and Y. Kuroda, *Adv. Powder Technol.*, 2013, **24**, 160–167.
46 C. Baumanis, J. Z. Bloh, R. Dillert and D. W. Bahnemann, *J. Phys. Chem. C*, 2011, **115**, 25442–25450.
47 A. Fujishima, T. N. Rao and D. A. Tryk, *J. Photochem. Photobiol., C*, 2000, **1**, 1–21.
48 D. Bauer, L. D'Ottone, P. Campuzano-Jost and A. J. Hynes, *J. Photochem. Photobiol., A*, 2003, **157**, 247–256.
49 B. Show, N. Mukherjee and A. Mondal, *RSC Adv.*, 2016, **6**, 75347–75358.
50 M. M. Rahman, A. Jamal, S. B. Khan and M. Faisal, *J. Nanopart. Res.*, 2011, **13**, 3789–3799.
51 L. Tang, H. Feng, J. Tang, G. Zeng, Y. Deng, J. Wang, Y. Liu and Y. Zhou, *Water Res.*, 2017, **117**, 175–186.
52 S. A. Styler and D. J. Donaldson, *Environ. Sci. Technol.*, 2012, **46**, 8756–8763.
53 H. A. Al-Abadleh, *RSC Adv.*, 2015, **5**, 45785–45811.
54 B. Aguila, Q. Sun, J. A. Perman, L. D. Earl, C. W. Abney, R. Elzein, R. Schlaf and S. Ma, *Adv. Mater.*, 2017, 1700665.
55 B. Li, Y. Zhang, D. Ma, Z. Shi and S. Ma, *Nat. Commun.*, 2014, **5**, 5537.